Intrinsic Image Decomposition-Based Grey and Pseudo-Color Medical Image Fusion

JIAO DU[1], **WEISHENG LI**[2], **AND HELIANG TAN**[1]

[1]School of Computer Science and Educational Software, Guangzhou University, Guangzhou 510006, China
[2]Chongqing Key Laboratory of Computational Intelligence, Chongqing University of Posts and Telecommunications, Chongqing 400065, China

Corresponding author: Jiao Du (dujiao19880429@126.com)

ABSTRACT It is difficult to extract both structural and functional information from the input grey magnetic resonance imaging (MRI) and pseudo-color positron emission tomography (PET) images using the same decomposition scheme in multi-scale transform fusion methods. To overcome this limitation, we propose two algorithms based on intrinsic image decomposition to decompose MRI and PET images into its two separate components in the spatial domain. Algorithm 1 could extract structural information while reducing the noise from the MRI image. Algorithm 2 is for averaging the color information from the PET image. As for the image fusion rule, the defined importance of image coefficients is used to combine the decomposed two-scale components to produce the final fused image, which could keep more spatial resolution with substitution strategies. It demonstrates that the proposed fusion methods could improve the values of mutual information by the metrics on the disease database. Furthermore, the proposed methods produce the competitive visual signal-to-noise ratio values on experiments for robustness database. In addition to the variance in metrics values, the non-parametric Friedman test and the post-hoc Bonferroni-Dunn test are used to analyze the significant difference between the proposed and the state-of-the-arts methods.

INDEX TERMS Two-scale MRI-PET fusion, intrinsic image decomposition, structural and functional information, statistical significance test.

I. INTRODUCTION

Medical image has witnessed a rapid growth in recent decades, i.e. computer tomography (CT), magnetic resonance imaging (MRI), positron emission tomography (PET), and single photon emission computed tomography (SPECT). Anatomic and functional information are essential for diagnosis in oncology for head tumors. In 1998, PET/CT scanner is introduced combining anatomic CT imaging and functional PET imaging in a single image. The huge success of PET/CT imaging is a proof of the strong interest in medical image fusion. Compared to PET/CT imaging, PET/MRI imaging includes additional advantages: (1) It provides high-resolution MRI image for studying abnormal brain structure and low-resolution multispectral PET image for studying metabolism information of brain. (2) The radiation dose is reduced. (3) The scanning time is reduced [1]–[3].

The associate editor coordinating the review of this manuscript and approving it for publication was Weiyao Lin.

Notably in this paper, MRI image is presented in grey. And, PET image is presented in pseudo-color.

PET/MRI medical image fusion is to merge multiple images with different features, such as anatomic and functional information. The purpose of medical image fusion is to preserve the specific features for increasing applications in handling with medical problems [4]. Nowadays, a broad range of medical image fusion methods are available in research institutes and hospitals worldwide. According to the representation format of processed image information, the image fusion methods could perform at pixel-level, feature-level, and decision-level, for respectively [5], [6]. Numerous research papers focus on medical image fusion at pixel-level using raw image pixel values. Therefore, we focus on the image fusion methods at pixel-level. Two aspects can be explored in pixel-level fusion methods: advanced image decomposition schemes and advanced image fusion rules [5]. According to the advanced image decomposition schemes, prospective methods for image fusion at pixel-level

can be roughly grouped into three categories: (1) single-scale methods [7]–[12], (2) multi-scale transform (MST) methods [13]–[25], and (3) two-scale methods [26]–[31].

The first category refers to measure the activity level of input raw images in a single-scale feature space for combining image coefficients. Principle component analysis (PCA) [7]–[9] based methods refer to the linear combination of vectors constructed from the input source medical images to form new irrelevant principle components. Fuzzy logic [10] is used to measure the local feature of the image in which the sharper edge in the image corresponds to the higher value of fuzzy logic. Furthermore, dense scale-invariant feature transform (DSIFT), a local feature descriptor, is introduced to extract the salient feature from the input images [11]. Due to that the higher intensity corresponds to the higher contrast, the intensity component of low-resolution PET image is replaced by higher-resolution MRI image using intensity-hue-saturation (IHS) [12] method. However, single-scale based methods introduce artificial effects, such as block effects and ringing effects.

The second category refers to MST including pyramid transform (PT) and wavelet transform (WT) performed in the transform domain. MST methods decompose inputs into low and high frequency bands. To begin with, Laplacian pyramid transform (LAP) [13] has been used to decompose the input image into a low frequency band and many high frequency bands. Next, Zheng *et al.* [14] builds a new advanced PT scheme using support value transform (SVT). Similarly, the salient features of the input source images can be obtained by the neighbor distance (ND) filter [15], as well. With the development of MST, WT has been identified as an ideal method for fusing images. Examples of these methods include discrete wavelet transform (DWT) [16], [17], curvelet transform (CVT) [18], contourlet transform (COT) [19], [20], non-subsampled contourlet transform (NSCT) [21], shearlet (ST) [22]–[25], etc. Especially, ST provides a true two-dimension spare representation for images with edges using a tight frame of well localized waveforms at different scales and directions. Wang *et al.* [25] firstly explored to use ST in the field of medical image fusion. However, MST based methods produce noisy fused images.

The third category is to construct a fast two-scale image decomposition scheme performed in the spatial domain for image fusion. Unlike MST based fusion methods performed in the transform domain, two-scale image decomposition scheme focuses on processing its raw image pixels in the spatial domain. And two-scale image decomposition scheme divides the inputs into smooth and detail parts. Shutao *et al.* [26] constructs the salient feature weighted map of the input source images using an edge-preserving smoothing filter: GFF [27], which can blur the detail information while preserving the edge information of the input images. Inspired from edge-preserving filter, the smooth layer is defined as the averaging of local minima and maxima envelops [28], [29]. And the detail layer is obtained by the subtraction of smooth layer from the input medical image.

Furthermore, the input image is decomposed into two layers with spatial feature and spectral feature using retina-inspired models (RIM) [30]. With the consideration of psychological and physiological mechanisms of the human visual system, internal generative mechanism (IGM) is proposed to decompose the input image into smoothed and detailed images [31]. However, the fused image that is obtained by two-scale based methods [28]–[31] is with low contrast.

Recently, the existing image fusion method combined with the image enhancement is used to obtain a final fused image with high-contrast detail information, simultaneously. Kou *et al.* [32] applies the gradient domain weighted least square (GWLS) after the pyramid transform-based fusion to enhance the details. Zhao *et al.* [33] uses adaptive gain function as the fusion rule for the detail images results from the total variation multi-scale decomposition method. Jang *et al.* [34] and Rahman *et al.* [35] constructs the multi-scale scheme using Retinex to obtain the image fusion and image enhancement. Inspired by these works in [32]–[34], the intrinsic image decomposition (IID) used as the multi-scale image decomposition scheme is proposed for the fusion of MRI and PET medical images in this paper. By the proposed method, the final fused image with enhanced detail information is obtained. Generally, the limitation of advanced image decomposition schemes is that the same scheme is adopted to decompose different source medical images. For the problem of image decomposition schemes, we construct two models of perceiving function of human vision to decompose input MRI and PET images into their two-scale detail-enhanced image representations by IID methods [8], [34]–[38] in this paper. Two directions of the new IID methods are the advanced reflectance estimation and the advanced illumination estimation methods [39]. Algorithm 1 [34], [35] based on Retinex method is used to estimate high-quality illumination image which is good at extracting salient information while reducing the noise from MRI image in grey. And Algorithm 2 [37] based on Grey-world method is used to estimate high-quality reflectance image by extracting the color information from a PET image in pseudo-color. For the problem of image fusion rules, PCA [9], the importance of image coefficients (IIC) [10], and intensity-hue-saturation (IHS) [12], which could keep more spatial resolution with substitution strategies, are selected as the image fusion rules for combing the decomposed two-scale images that are obtained by IID methods. The advantages of the proposed methods are shown as follows:

(1) MST based fusion methods require more than two scales. This paper presents a simple two-scale fusion method performed in the spatial domain using two different IID methods for the input two medical images. Hence, the reflectance and illumination layers obtained via IID methods could preserve much more detail information.

(2) Inspired by the work in [10], the Dempster-Shafer (D-S) evidence theory is used to evaluate the important information in the decomposed reflectance and

illumination image. Compared to the existing fusion framework, the final fused image is obtained by performing IIC based fusion rule on all the decomposed images at various scales from the inputs.

(3) The experimental results illustrate both subjective and objective evaluations on the testing imaging data with respect to resolution changes, motion artefacts and synthetic noise. This paper gives a discussion on the values of the selected full-reference image quality metrics using non-parametric tests for judging whether there exists a significant difference between the state-of-the-arts and proposed fusion methods.

The remainder of the paper is organized as follows. In Section II, the theory of IID and its related research works: Retinex and Grey-world methods are described. In Section III, the proposed fusion methods based IID are illustrated. Section IV gives the experiments. Finally, the conclusion is shown in Section V.

II. INTRINSIC IMAGE DECOMPOSITION

Intrinsic image decomposition (IID) is defined as the problem of separating an image into its reflectance and illumination components [36]. The IID problem can be defined as follows:

$$I = R + L \qquad (1)$$

where I denotes an input image, R denotes the reflectance component corresponding to the intrinsic reflectivity of a surface, and L denotes the illumination component referring to the illumination of the scene and texture of the objects. The high-quality reflectance and illumination components are recovered from a single image using Retinex and Grey-world based methods.

A. RETINEX-BASED METHODS

Decomposition with a single image is studied using Retinex-based method in this paper. Retinex method simulates the human visual system and explains the color constancy phenomenon. The primary goal of Retinex-based methods is to decompose one image into a reflectance image and an illumination image [34], [35]. Taking a digital image I as an input, the output of the method is the reflectance image R on a pixel by pixel in the following manner:

$$R(x, y) = \log(I(x, y)) - \log(I(x, y) * F(x, y)) \qquad (2)$$

where $*$ denotes spatial convolution operation and

$$F(x, y) = \alpha \exp\left(-\left(x^2 + y^2\right) / \sigma^2\right) \qquad (3)$$

in which σ is the scale factor that controls the width of the kth surround function and α is the normalization factor. Fig. 1 gives the input grey image and its corresponding reflectance images using three scale factor values. The input natural image in greyscale in Fig. 1(a) presents noise structural information of tissues and organs. To increase contrast of the image, the single scale Retinex (SSR) method is applied on the input MRI with different scale parameters, displayed
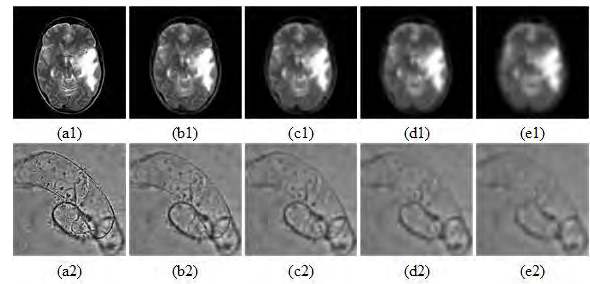

FIGURE 1. The input MRI and its results of scale factor with different values ($\sigma = 5, 11, 25$).

in Fig. 1(b)-(d). Fig. 1(b) ($\sigma = 5$) displays high-contrast foregrounds characterized by enhanced illumination of white matter. Fig. 1(c) ($\sigma = 11$) presents clear shape information around the boundary and introduces much more illumination. And, Fig. 1(d) ($\sigma = 25$) presents high-contrast illumination but the modified structural information of white matter from the input MRI. That is, the parameter σ determines the contrast of the reflectance image. The larger σ retains more detail information of the white matter characterized by higher-contrast illumination. On the other side, the smaller σ means the more spatial detail information of the structural information. The scale factor is used to balance structural information and white matter.

Fig. 2 displays four examples of image decomposition results applying different values of the scale factor ($\sigma = 5, 13, 11, 7$) by Retinex-based method. From Fig. 2, it can be cleared that the four different types of images: the woman, the man, CT and MRI are respectively decomposed into a reflectance component and an illumination component. The former preserves the primary visual information of the source image, such as structural information. On the other hand, the latter preserves the illumination information, such as the high contrast in the latter part.

B. GREY-WORLD-BASED METHODS

Grey-world method is another developed to address the problem of color constancy. In human visual system, light is received by the eyes which send signals to the visual cortex. And color constancy is a process described as the procedure of allowing the human brain to recognize a familiar object as being a consistent color regardless of the amount of light reflecting from it at a given moment [37]. The pixel values of the input RGB (red, green, blue) color image are dependent on the light source, the surface reflectance and the camera sensitivity function. Grey-world method estimates the illumination component by the average color of the selected image resulted from the color constancy [40].

$$\int R(\lambda, I(x, y)) dI(x, y) / \int dI(x, y) = c \qquad (4)$$

where λ is the wavelength, $I(x, y)$ denotes each pixel at the location (x, y), $R(\lambda, i)$ is the surface reflectance and c is a constant setting by the average values of separate channels
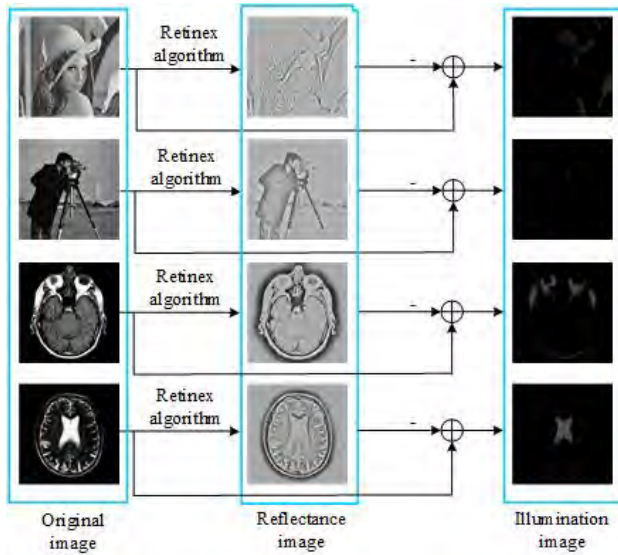
FIGURE 2. Four examples of intrinsic image decomposition method: Retinex-based method ($\sigma = 5, 13, 11, 7$).
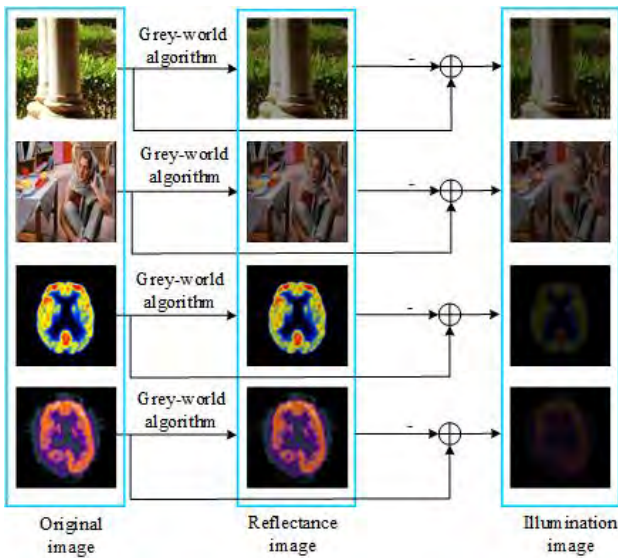

FIGURE 3. Four examples of intrinsic image decomposition method: Grey-world algorithm.

in the color image. Using Grey-world method in the image processing, the original intrinsic image is recovered by eliminating the reflection of the light. Fig. 3 shows four examples of image decomposition using Grey-world method. From the Fig. 3, it can be observed that each source image is separated into a reflectance component and an illumination component. Compared to Retinex method, the reflectance part filtered by Grey-world method looks more like the source image. Furthermore, as for the color source images, the first one shows good visibility and discards the color shifting, the second one is obtained by subtracting the reflectance image from the source image according to Eq. (1). In the illumination image, it is with high contrast.

TABLE 1. Important notation and terms used in this paper.

I_A, I_{A1}, I_{A2}	Input source MRI image, reflectance and illumination parts of MRI image, respectively.
I_B, I_{B1}, I_{B2}	Input source PET image, reflectance and illumination parts of PET image, respectively.
I_F	Fused image from MRI and PET images.
C, S, F	Cartoon, smoothed, and result images after Gaussian filter.
RS, LS	Reflectance and illumination images of smoothed image, respectively.

III. PROPOSED MRI AND PET IMAGES FUSION METHODS
A. INPUTS

Please refer to Table 1 for important definitions used throughout the rest of this paper. The inputs are MRI and PET medical imaging data. According to the standard of imaging system, medical imaging data can be divided into structural and functional image. MRI, structural image, provides information about the tissue type of the human brain. PET, functional image provides better information on blood flow and flood activity with low space resolution in general. For PET image, functional information is likely to result in changes in apparent shape during acquisition as the tracer redistributes. The fusion of MRI and PET images aims to preserve both the detailed image of anatomical structures of the human brain and image-wide quantification of physiological and biochemical processes within the body. The input source images are assumed to be co-registered.

B. TWO-SCALE IMAGE DECOMPOSITION

Due to the properties of images with different modalities, Algorithm 1 and Algorithm 2 are applied to MRI and PET images to get their two-scale image representations, respectively. Algorithm 1 built on Retinex method is good at recovering reflectance from MRI while reducing noise. In pseudo-color PET image, the correlation between three channels is helpful for tracing tumors. Therefore, Algorithm 2 built on Grey-world method is used to extract the high-intensity information of the image with color constancy.

Inspired from the smoothed L_1-Retinex method illustrated in the paper [41], the MRI images are decomposed into their two-scale image representations of illumination and

---

Algorithm 1 Intrinsic Image Decomposition – MRI

Input: MRI image I_A
Output: Reflectance image I_{A1} and illumination image I_{A2}
1. Apply the defined low-pass filter F_L on I_A to get cartoon image C
2. Smoothed image: $S = C$
3. Reflectance image of smoothed image:
   $R_S = (R + G + B)./3$
4. Illumination image of smoothed image: $L_S = S - R_S$
5. Illumination image: $I_{A2} = L_S$
6. Reflectance image: $I_{A1} = I_A - I_{A2}$

Algorithm 2 Intrinsic Image Decomposition – PET

Input: PET image I_B
Output: Reflectance image I_{B1} and illumination image I_{B2}
1. Apply Gaussian filter on image I_B to get filtered image I'_B
   $I'_B = imfilter(gaussian, I_B)$
2. Apply color consistency on the filtered image I'_B to get reflectance image I_{B1}

$$I_{B1} = (R * \frac{(\overline{R} + \overline{G} + \overline{B})/3}{\overline{R}}, G * \frac{(\overline{R} + \overline{G} + \overline{B})/3}{\overline{G}},$$
$$B * \frac{(\overline{R} + \overline{G} + \overline{B})/3}{\overline{B}})$$

3. Illumination image: $I_{B2} = I_B - I_{B1}$

---

reflectance images by Algorithm 1. In medical images such as MRI, the digital signals sometimes are corrupted by bias field. It is a good idea to apply Retinex method for recovering the reflectance image from the original signals. The assumption of Algorithm 1 is that illumination image equals to the illumination of the smoothed image. Firstly, the smoothed image of input images is obtained from the cartoon part C using the defined low-pass filter in [42] with the local window size ($\sigma = 3$),

$$C = w(\sigma) \left(F_L^\sigma * I_A \right) + (1 - w(\sigma)) I_A \quad (5)$$

where $w(\sigma)$ denotes the increasing weighted function. Then, the reflectance image of smoothed image is computed by averaging the channel information to get. Consequently, the reflectance image is recovered by subtracting the illumination of the smoothed image from the original medical MRI image.

Since pseudo-color PET image provides significant details of the lesion region in human brain, the goal of **Algorithm 2** is to separate the original PET medical image into reflectance image containing the normal regions and illumination images containing the lesion regions. On the assumption of color constancy, Grey-world algorithm is applied to the pseudo-color PET image for discovering the lesion region. Because of the input PET image destroyed by the noise, the input PET image is firstly smoothed using Gaussian filter firstly to get high-quality intrinsic images. Then, the color constancy is defined as the grey value by averaging of R, G and B channels. The illumination image is estimated by the ratio of the grey value to the average value of the image matrix with the separated color channel. Finally, the reflectance image is obtained by the difference between the input image and the illumination image.

C. IMAGE FUSION RULES
Image fusion rules refer to algorithms that seek to highlight the features of interest in images and restrain the features of insignificance. The main contribution of fusion rules is the combination of multiple images into a single image [5]. Effective fusion rules are closely related to the quality of the fused image. Usually, the averaging-maximum scheme

has been widely used to produce the fused coefficients. This scheme, however, loses spatial information [23], [25]. Therefore, PCA, IIC and IHS [9], [10], [12] are chosen as the image fusion rules for combining the decomposed images by Algorithm 1 and Algorithm 2 with the advantages of implementing using a simple operation on image pixels in spatial domain. PCA is the combination of principal components from two decomposed images which refers to the linear combination of vectors forming new irrelevant principal components. Based on D-S evidence theory, IIC is performed on the four decomposed image coefficients I_{A1}, I_{A2}, I_{B1} and I_{B2} simultaneously to obtain the final fused image I_F, expressed as,

$$I_F = \sum_{i \in \{A1, A2, B1, B2\}} \frac{[w_i(x, y) * I_i(x, y)]}{w_i} \quad (6)$$

where the weight w for importance coefficient of each image is calculated by [25],

$$w_i = \frac{1 - c_i}{\max\{1 - c_{A1}, 1 - c_{A2}, 1 - c_{B1}, 1 - c_{B2}\}} \quad (7)$$

where the function max is used to get the maximum value among the input parameters. And the correlation of the image c_I is defined as,

$$c_i = d_i / \sum_{i \in \{A1, A2, B1, B2\}} d_i + c \quad (8)$$

where the difference of every decomposed image d_i is obtained from the percentage of the total Euclidean distance of the image ($d_i = \sqrt{\sum_{i \in \{A1, A2, B1, B2\} \cap i \neq j} (I_i - I_j)^2}$). In IIC, the greater the variance among the decomposed components, the higher value the decomposed image gets. In IHS, the low resolution in PET is replaced by a grey MRI image with higher spatial resolution by which the fused image can keep the same spatial resolution as the original high-resolution image.

D. PROPOSED METHODS
Figs. 4 summarize the main processes of specific fusion examples. Firstly, Algorithm 1 and Algorithm 2 are utilized to get the two-scale image representations. The IID used as the two-scale image decomposition scheme is proposed in this paper. The decomposed reflectance image denotes the outline information of the input grey MRI and pseudo-color PET images. And the decomposed illumination image denotes the high-intensity information of the input images. Then, the decomposed layers are combined into a single image using PCA, IIC, and IHS based fusion rules for preserving much more spatial information, respectively. (1) IID+PCA based fusion method: As shown in Fig. 4, the input MRI and PET images are firstly decomposed into its corresponding reflectance and illumination images by Algorithm 1 and Algorithm 2, respectively. The fused reflectance image I_F^1 that is obtained by the PCA based fusion rule is similar in pseudo-color information to the decomposed reflectance image of the input PET image. The fused illumination image
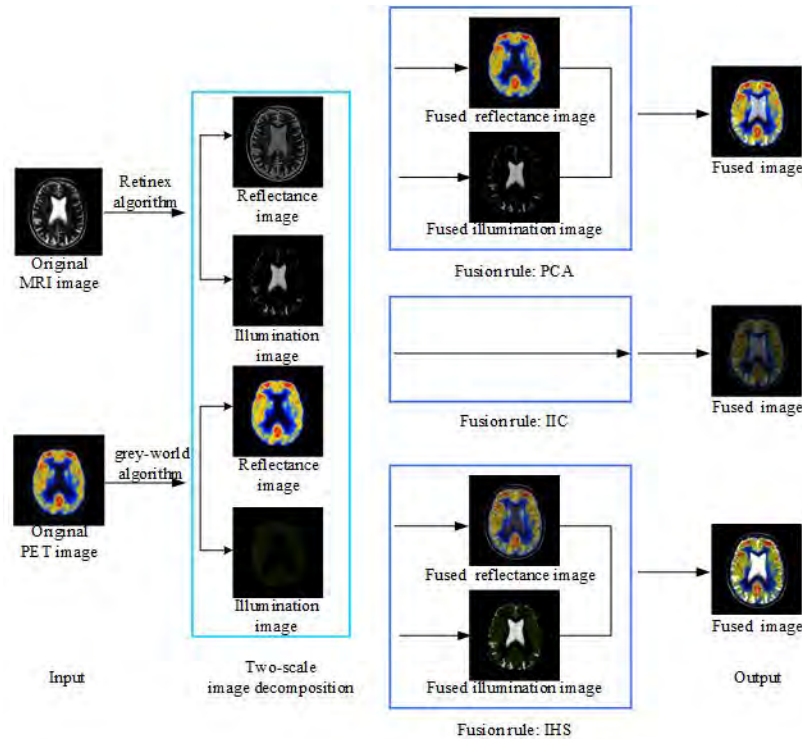
FIGURE 4. Schematic diagram of the proposed image fusion methods: IID+PCA, IID+IIC and IID+IHS.

I_F^2 that is obtained by the PCA based fusion rule is similar in high-intensity grey matter of the brain to the decomposed illumination image of the input MRI image. (2) IID+IIC based fusion method: To combine two-scale representations of input MRI and PET images, IIC is proposed as the rule for the reflectance and illumination images on the assumption that the fused image is composed of the uncertain proportion of image coefficients from the decomposed image inputs. In Fig. 4, the four decomposed inputs are combined into the fused image using the weighted average calculated by the D-S theory. The fused image presents low-intensity color information. (3) IID+IHS based fusion method: The input images are presented by their reflectance and illumination images. To preserve high-intensity information, IHS based fusion rule is applied to obtain both the fused reflectance image and the fused illumination image. Notably, the fused illumination image and shows high-intensity white matter of the brain, shown Fig. 6. The fused reflectance image presents high-contrast detail information, such as the textural information. And then, the final fused image is obtained by addition of the fused reflectance image I_F^1 and the fused illumination image I_F^2. In Fig. 4, the fused image not only preserves the intensity information from the input images but also enhances the contrast.

IV. EXPERIMENTS
A. EXPERIMENTAL SETTINGS
1) BASIC SETTINGS
The experiments are performed on two databases, i.e., disease database which contains 30 pairs of abnormal brain

from Harvard University [44] and the clinical cases [45], and the second database provided for analysis of robustness which includes 6 pairs of images with resolution changes (3 pairs for fusing MRI and PET images with the resolution of 128×128 and 3 pairs with the resolution of 512×512, respectively), 6 pairs with motion artifacts, and 6 pairs with synthetic noise. The purpose of disease and robustness databases in subsections IV.B and IV.C is to verify the performance the experimental results on the standard data and the artificial data, respectively. The testing imaging data contains high resolution MRI images and pseudo-color PET images with the resolution of 256×256 except for the resolution changes sets. The corresponding pixels of MRI and PET image have been co-registered. From the input source images in figures, it can be noticed that MRI image captures the anatomical structure information of the human brain, while it fails in displaying functional information. In contrast, PET image reflects the blood flow changes in apparent shape acquisition clearly, while hardly shows bones of human brain. In addition, the proposed methods are compared with eleven image fusion methods based on LAP [13], DWT [16], CVT [18], COT [19], NSCT [21], ST [23], SVT [14], GFF [26], ND [15], LES [29], and DSIFT [11]. The compared fusion methods include two categories: methods performed in the transformed domain and in the spatial domain. LAP, DWT, CVT and COT methods apply sampled resolution sizes in the transformed domain. NSCT, ST, SVT and ND methods apply the same resolution sizes as the input images for reducing block effects in the transformed domain. On the other side, LES
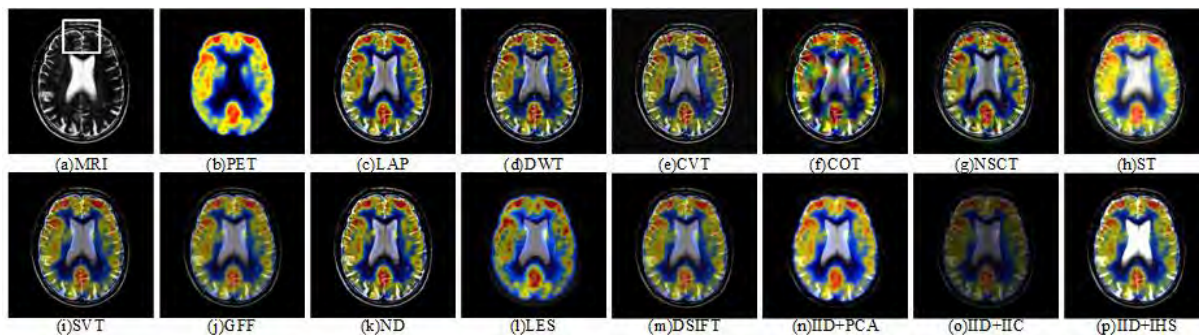
FIGURE 5. One example of result images with Mild Alzheimer's disease by different fusion methods.
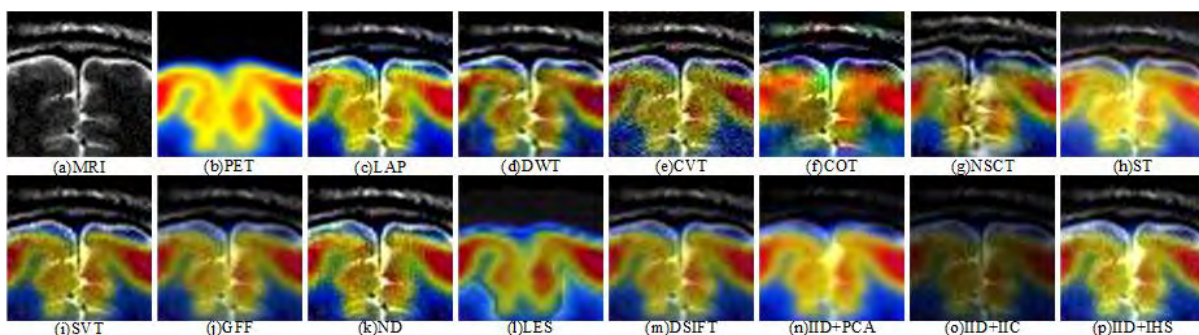

FIGURE 6. Zoom regions of one example result images with Mild Alzheimer's disease.

and DSIFT methods employ salience feature descriptors as the advanced image decomposition scheme and image fusion rule. In this paper, full-reference metrics based on human visual system (i.e. structural similarity (*SSIM*) [46], information content weighted *SSIM* (*IWSSIM*) [47], mutual information (*MI*) [48], gradient similarity scheme (*GSM*) [49], and visual signal-to-noise ratio (*VSNR*) [50], [51] metrics) are adopted for evaluating the quality of fused images. The bigger the metrics *SSIM*, *IWSSIM*, *MI*, *GSM*, and *VSNR* are, the better the fused images are.

B. EXPERIMENTAL RESULTS ON DISEASE DATABASE

Fig. 5 shows one example of abnormal brain images with Mild Alzheimer's disease. By carefully observing the fused images in Fig. 5, it can be noticed that the brain structures in Fig. 5(c), (j), (k) and (p) are perfectly captured as what they like in Fig. 5(a). And the functional information is completely preserved in the result images by SVT and IID+IHS fusion methods in Fig. 5(i) and (p). In Fig. 5(f), (g), and (l), the result images produce obvious color distortion. In Fig. 5(m) and (o), the result images show low contrast. In addition, by comparing the zoom regions of the result images in Fig. 6, the proposed IID+IHS method works better in preserving both edge and texture information from the source images.

Figs. 7-8 show the MRI and PET input images with Glioma disease. From Fig. 7(f), (g), and (n), the result images obviously introduce color distortion using COT, NSCT and IID+PCA methods. However, the white region is better preserved by IID+PCA method than that by COT and NSCT methods. The result images completely preserve the structural information using DWT, ND, and DSIFT methods in Fig. 7(d), (k), and (m). Furthermore, the intensity of PET image directly relates to the saliency information of the tissue. Higher intensity information can be observed in the result images using IID+IHS method in Fig. 7 (p). By carefully observed the zoom regions in Fig.8, the ND and IID+IHS methods work better in combing structural information and intensity information.

Next, Figs. 9-10 show two clinical cases of neurologic disease to demonstrate the availability of the proposed methods. Simultaneous acquisition fused images from MRI and PET image are shown in Fig. 9 (c)-(p) and Fig. 10(c)-(p). In the first case, the background of results images is not clear using DSIFT and IID+IIC methods in Fig. 9(m) and (o). SVT and IID+IHS methods introduce higher intensity information which indicates greater activity of the tissues. In the second case, the result image presents structural information in low resolution using GFF method in Fig. 10(j). Color distortion exists in the result image using COT method in Fig. 10(f). In addition, SVT, IID+PCA, and IID+IHS methods preserve both brain structure and blood tissues from source images in Fig. 10 (i), (n), and (p).

Lastly, Table 2 shows the quantitative assessment of different image fusion methods on disease database in terms of
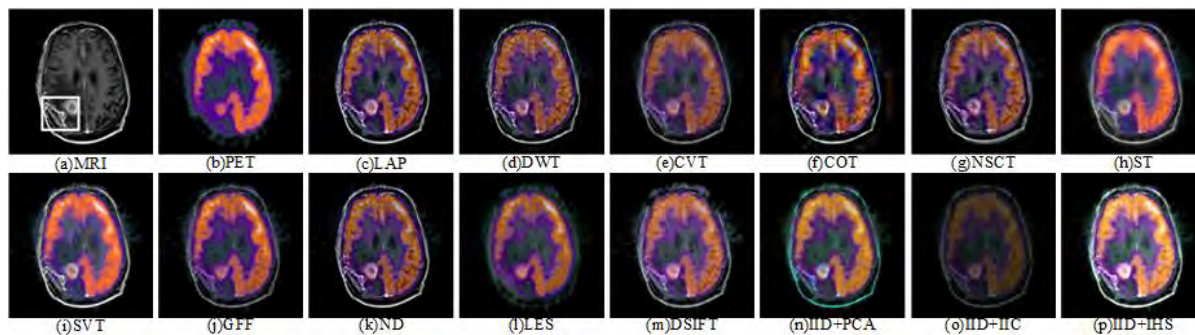
FIGURE 7. One example of Result images with Glioma disease by different fusion methods.
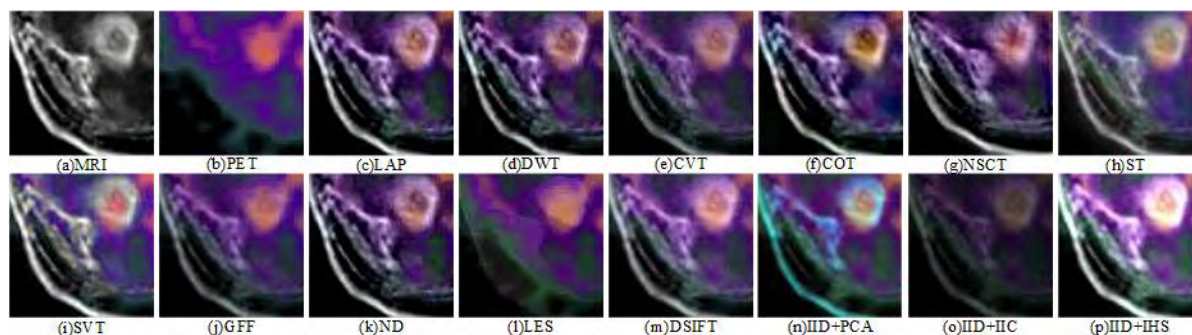
FIGURE 8. Zoom regions of one example result images with Glioma disease.
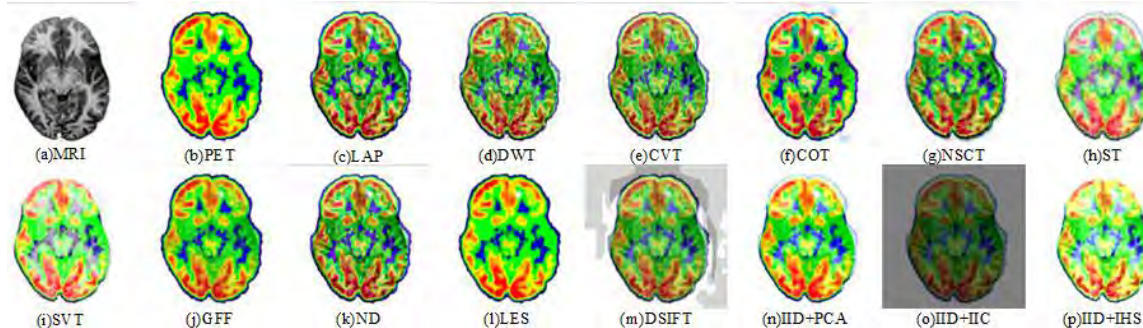
FIGURE 9. The first clinical case of MRI-PET fusion for neurologic application.

SSIM, *IWSSIM, MI, GSM* and *VSNR* metrics [40]–[45]. The mean (Mean) and standard deviations (Std) values of objective metrics are listed in Table 2, where the best metric has been highlighted in bold. From Table 2, it can be obviously observed that the proposed methods perform better in terms of four metrics: *IWSSIM, MI, GSM,* and *VSNR*. Moreover, the *MI* value of the proposed IID+IHS method is the largest over 30 pairs of the input MRI and PET image. That is, IID+IHS method can well preserve the original information from the original source images. On the other hand, LAP method gets the best Mean value for the metric *SSIM*.

C. EXPERIMENTAL RESULTS ON ROBUSTNESS DATABASE
The resolution changes and motion artifacts often occur in MRI and PET images [52]. Fig.11 illustrates the performance

of methods for fusing MRI and PET images of resolution 128×128. The result images perfectly combine both structural information and intensity information using LAP, ND, and IID+PCA methods. In Fig. 11(l), the fused image loses much more structure information of eyes from the input MRI image, compared to the other fusion methods. Higher intensity information can be found in the fused images using SVT, DSIFT, and IID+IHS methods. However, color distortion can be easily observed in fused images using COT and NSCT methods in Fig. 11(f) and (g).

In addition, Fig. 12 illustrates an example of reducing motion artifacts in fused MRI/PET images. Fig.12 (a) shows the input MRI image corrupted by motion artifacts, while PET image dose not in Fig. 12(b). The results are displayed in Fig. 12(c)-(p). The results are blurring using ST, SVT, ND,

FIGURE 10. The second clinical case of MRI-PET fusion for neurologic application.

TABLE 2. Performance comparison of fusion methods in terms of five metrics on disease and robustness databases.

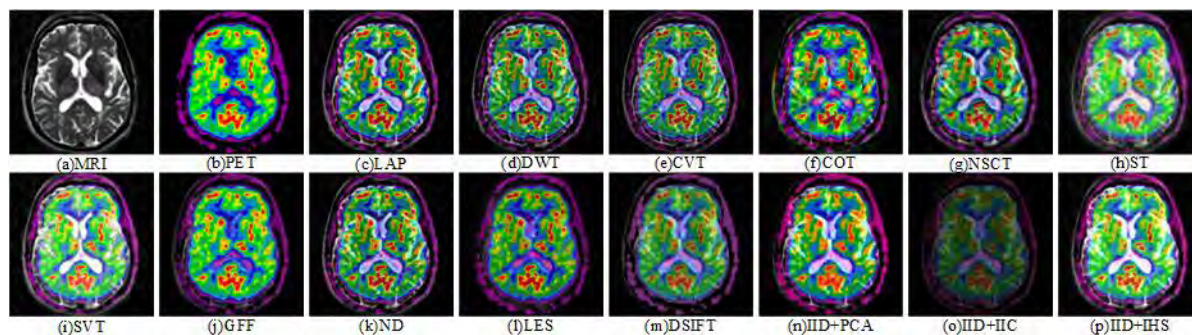| Disease		LAP	DWT	CVT	COT	NSCT	ST	SVT	GFF	ND	LES	DSIFT	IID+PCA	IID+IIC	IID+IHS
SSIM	Mean	**0.6086**	0.5624	0.4955	0.3191	0.3267	0.4572	0.6018	0.5969	0.6021	0.5272	0.6002	0.5603	0.5109	0.5891
	Std	0.1462	0.1300	0.1748	0.0345	0.1369	0.1113	0.1344	0.0974	0.1471	0.1815	0.1404	0.1600	0.1451	0.1489
IWSSIM	Mean	0.6354	0.6333	0.6408	0.5879	0.5089	0.6357	0.6209	0.6050	0.6294	0.5719	0.5496	**0.6413**	0.5014	0.6301
	Std	0.0500	0.0623	0.0662	0.0692	0.0591	0.0613	0.0541	0.0583	0.0588	0.0723	0.0753	0.0645	0.0680	0.0503
MI	Mean	4.7602	4.6347	4.7384	4.3058	4.3065	4.8173	5.0244	4.9059	4.7347	4.8062	4.9927	4.8601	4.5164	**5.1446**
	Std	0.4827	0.4775	0.4581	0.4115	0.4660	0.5072	0.5515	0.5847	0.4781	0.5481	0.5039	0.5970	0.4986	0.5652
GSM	Mean	0.9796	0.9791	0.9801	0.9773	0.9702	0.9798	0.9796	0.9811	0.9794	0.9789	0.9771	**0.9811**	0.9761	0.9787
	Std	0.0052	0.0052	0.0078	0.0056	0.0077	0.0052	0.0053	0.0043	0.0053	0.0054	0.0061	0.0054	0.0074	0.0053
VSNR	Mean	10.7429	12.6996	14.6524	10.6995	11.3465	10.1419	6.5183	16.4015	11.2667	17.7695	8.4276	10.7812	**27.6106**	6.1340
	Std	1.5325	1.6110	2.2408	1.4792	1.2309	2.5214	2.6874	4.3757	1.5446	3.0663	3.1650	2.0606	5.0374	2.6953
Robustness															
SIM	Mean	0.4602	0.4345	0.4399	0.2563	0.2598	0.3575	**0.4733**	0.4383	0.4720	0.4138	0.4721	0.4462	0.4059	0.4670
	Std	0.2784	0.2588	0.2738	0.1329	0.1870	0.1837	0.2804	0.2679	0.2841	0.2752	0.2885	0.2546	0.2549	0.2654
IWSSIM	Mean	0.5210	0.5168	0.5254	0.4634	0.3771	0.5288	0.5180	0.5252	0.5226	0.4908	0.4919	**0.5474**	0.4758	0.5409
	Std	0.1220	0.1224	0.1211	0.0920	0.1005	0.0989	0.1183	0.1118	0.1204	0.0993	0.1155	0.1110	0.0905	0.1174
MI	Mean	4.2927	4.0797	4.1936	3.8685	3.7770	4.2996	4.5322	4.3020	4.1666	4.2748	4.3392	4.4026	3.9697	**4.5844**
	Std	1.1384	1.0532	1.0721	0.9044	0.9756	0.9416	1.1113	1.1647	1.0850	1.0436	1.1802	1.0047	0.9178	1.0879
GSM	Mean	0.9390	0.9383	0.9457	0.9383	0.9390	0.9543	0.9395	0.9505	0.9392	0.9556	0.9390	0.9566	**0.9645**	0.9495
	Std	0.0545	0.0541	0.0467	0.0514	0.0390	0.0324	0.0530	0.0425	0.0543	0.0392	0.0524	0.0374	0.0137	0.0393
VSNR	Mean	9.7846	10.5526	11.9737	9.5859	9.7663	7.5330	4.5940	14.3118	9.5676	14.9900	11.5562	10.2670	**26.7091**	6.3294
	Std	3.2489	3.4288	4.3011	3.0831	1.4370	2.5532	1.8326	4.9388	3.1388	4.8364	8.5256	3.4097	3.7197	1.3858
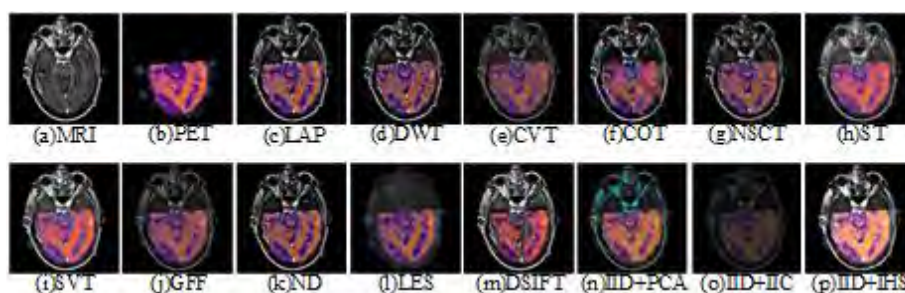
FIGURE 11. Fusion results of resolution changes.

TABLE 3. Averaged running time of different methods (s).

LAP	DWT	CVT	COT	NSCT	ST	SVT	GFF	ND	LES	DSIFT	IID+PCA	IID+IIC	IID+IHS
0.07	0.08	0.94	0.57	52.89	70.02	0.10	0.67	1.22	17.46	3.36	**0.05**	**0.05**	0.07

and IID+IHS methods. However, from Fig. 12 (l), the quality of the fused image is not deteriorated by MRI image using LES method. IID+PCA method presents good statistics in Fig. 12(n). When simulating method, it is important to add synthetic noise to the input data to accurately model performance. Therefore, we show the performance of fusion
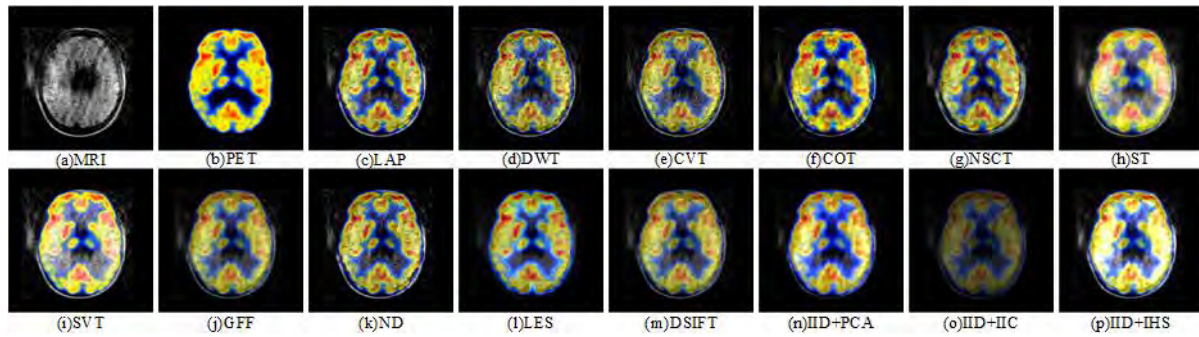
FIGURE 12. Fusion results of motion artifacts.
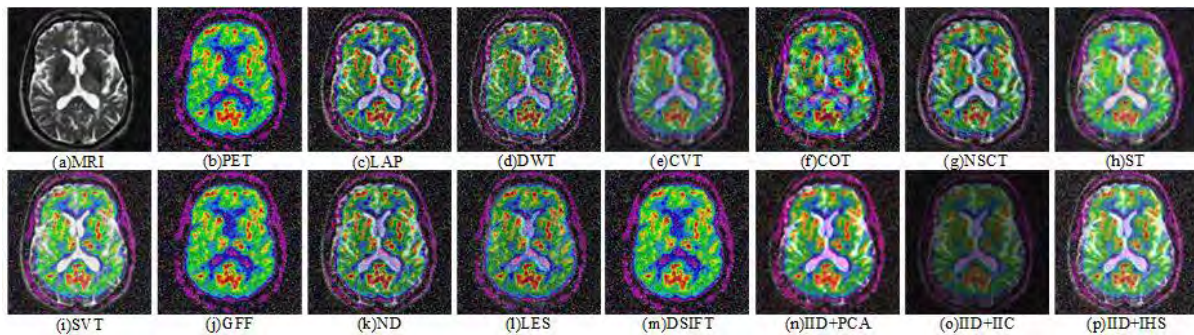
FIGURE 13. Fusion results of synthetic noise.

methods across four noise types including Gaussian noise (*variance* = 0.020), Poisson noise, salt-and-pepper noise (*density* = 0.20), and speckle noise (*variance* = 0.030) [53]. In Fig. 13, the result images using GFF and DSIFT methods looks the same as the input PET image. Unfortunately, the images using GFF and DSIFT methods are seriously destroyed by salt&pepper noise. Moreover, DWT and ND methods introduce enhanced detail information while adding noise from the inputs. COT and NSCT methods introduce color distortion. However, the proposed IID+PCA, IID+IIC, and IID+IHS methods are robust to noise due to that the background of the results is clear.

Lastly, for the three groups of medical images: resolution changes, motion artifacts, and synthetic noise, the detailed quantitative evaluations on robustness database are given in Table 2. Lines 7-11 in Table 1 display the values of the metrics *SSIM*, *IWSSIM*, *MI*, *GSM*, and *VSNR*. The highest value of the metric *IWSSIM* for the fused images indicates that the image components obtained by the proposed IID+PCA method contain more attracted visual information content. Similarly, the proposed IID+IIC method performs best in terms of *GSM* metric. Moreover, the fused image generated with the proposed IID+IIC method has less noise (higher *VSNR*) than the other result images.

D. COMPUTATIONAL COMPLEXITY ANALYSIS

Table 3 records the average running time of fourteen methods. Experiments are using MATLAB R2012a on a computer

equipped with a 3.30GHz CPU and 8GB memory. From Table 3, IID+PCA and IID+IIC methods run faster among the other methods. LAP and IID+IHS methods gets the second prize in the competition of running time. GFF, LES, DSIFT, IID+PCA, IID+IIC, IID+IHS methods perform in spatial domain, while LAP, DWT, CVT, COT, NSCT, ST, SVT, ND methods perform in frequency domain. The average time of methods in spatial domain is 3.61(s). However, the average time of methods in frequency domain is 15.74(s). The running time of ST (70.02 (s)) is the lowest because of the ST coefficients constructed by filter banks in frequency domain. The average running time of methods in frequency domain (LAP, DWT, CVT, COT, NSCT, ST, SVT, and ND) is longer than that in spatial domain (GFF, LES, DSIFT, IID+PCA, IID+IIC, and IID+IHS) in Table 3. COT method gets the first prize among the methods in frequency domain. But color distortion usually exists in the fused images using COT method.

E. DISCUSSIONS

30 pairs of images in Section IV.B and 18 pairs of images in Section IV.C are used to measure the performance of the proposed methods. However, we do not make a conclusion what the true translation performance is. Statistical significance is a tool to evaluate the true translation quality [54], [55]. Therefore, an extensive analysis (non-parametric Friedman test and the post-hoc Bonferroni-Dunn test) is provided in Table 4-6 for evaluating the statistical significance of the observed

TABLE 4. Ranking of competitor fusion methods, achieved by the Friedman test at two databases: disease and robustness.

Method	Disease					Robustness				
	SSIM	*IWSSIM*	*MI*	*GSM*	*VSNR*	*SSIM*	*IWSSIM*	*MI*	*GSM*	*VSNR*
LAP	**13.3**	11.1	8.3	10.2	5.3	10.6	8.5	9.3	7.6	5.8
DWT	6.9	10.0	4.8	7.0	9.7	7.0	7.1	5.4	10.5	8.3
CVT	7.2	11.5	6.6	11.0	11.0	7.6	9.6	6.3	5.6	10.4
COT	2.1	5.2	1.4	3.6	5.5	2.7	4.2	3.4	10.6	6.2
NSCT	1.5	1.8	1.8	1.1	7.2	1.4	2.0	1.7	4.0	7.5
ST	3.6	10.3	8.3	9.6	6.0	6.1	9.8	8.9	3.7	4.6
SVT	11.5	7.9	11.7	9.3	3.0	10.7	7.8	12.1	9.7	1.3
GFF	9.0	7.8	10.1	11.0	12.1	7.9	9.1	8.3	6.8	10.9
ND	11.7	8.8	7.0	8.9	7.2	10.7	8.6	7.5	7.5	6.4
LES	5.3	4.5	7.6	6.9	12.4	5.4	5.0	6.9	7.5	11.3
DSIFT	11.2	3.2	8.7	3.3	3.9	**11.3**	5.5	8.3	4.1	6.8
IID+PCA	7.0	**11.6**	11.8	**12.6**	6.2	7.9	11.0	10.1	**12.6**	7.9
IID+IIC	4.8	1.4	3.2	3.1	**13.6**	4.5	5.2	3.7	3.1	**14.0**
IID+IHS	9.9	9.8	**13.6**	7.3	1.9	11.2	**11.6**	13.1	7.3	3.6
Statistic	1.42E-58	1.27E-54	2.80E-57	9.77E-52	2.76E-57	3.57E-16	1.23E-23	2.66E-13	9.77E-52	1.51E-25
p-value	3.11E+02	2.98E+02	3.04E+02	2.78E+02	3.04E+02	1.38E+02	1.03E+02	1.41E+02	8.85E+01	1.51E+02

TABLE 5. Adjusted p-values on two databases using the post-hoc Bonferroni-Dunn test.

i	Hypothesis	adjusted *p-value*(Disease)					adjusted *p-value*(Robustness)				
		SSIM	*IWSSIM*	*MI*	*GSM*	*VSNR*	*SSIM*	*IWSSIM*	*MI*	*GSM*	*VSNR*
1	IID+PCA vs LAP	1	1	1	1	1	1	1	1	1	1
2	IID+PCA vs DWT	1	1	0.64097	1	0.634631	1	1	1	1	1
3	IID+PCA vs CVT	1	1	1	1	**7.08E-06**	1	1	1	1	1
4	IID+PCA vs COT	**6.27616E-09**	0.09309	**2.9E-05**	1	1	1	1	1	1	1
5	IID+PCA vs NSCT	**2.27457E-08**	**2.9E-13**	**3E-05**	**3.35E-10**	1	1	**0.000578**	1	1	1
6	IID+PCA vs ST	0.401174602	1	1	1	1	1	1	1	1	1
7	IID+PCA vs SVT	1	1	1	1	**3.43E-07**	1	1	1	1	**0.00233**
8	IID+PCA vs GFF	1	1	1	1	**1.76E-12**	1	1	1	1	0.223564
9	IID+PCA vs ND	1	1	1	1	1	1	1	1	1	1
10	IID+PCA vs LES	1	**0.00193**	1	1	**8.26E-19**	1	1	1	1	**0.038643**
11	IID+PCA vs DSIFT	1	**2.3E-06**	1	0.727973	0.08714	1	1	1	1	1
12	IID+PCA vs IID+IIC	1	**1E-14**	**0.03207**	0.102185	**5.11E-77**	1	1	1	1	**9.34E-26**
13	IID+PCA vs IID+IHS	1	1	1	1	**1.41E-08**	1	1	1	1	0.289271
14	IID+IIC vs LAP	0.625149654	**1.5E-13**	1	1	**2.98E-77**	1	1	1	1	**5.8E-27**
15	IID+IIC vs DWT	1	**3.7E-13**	1	1	**3.34E-65**	1	1	1	1	**4.8E-25**
16	IID+IIC vs CVT	1	**1.3E-14**	1	0.828449	**4.17E-53**	1	1	1	1	**1.49E-21**
17	IID+IIC vs COT	**1.4894E-05**	**1.3E-05**	1	1	**1.62E-77**	1	1	1	1	**1.84E-27**
18	IID+IIC vs NSCT	**4.34478E-05**	1	1	**0.010913**	**1.49E-73**	1	0.720697	1	1	**5.22E-27**
19	IID+IIC vs ST	1	**1.3E-13**	1	1	**6.53E-81**	1	1	1	1	**1.18E-32**
20	IID+IIC vs SVT	1	**7.4E-11**	**0.01281**	1	**2.4E-102**	1	1	1	1	**3.95E-40**
21	IID+IIC vs GFF	1	**3.6E-08**	0.30866	0.103431	**2.08E-42**	1	1	1	1	**4.84E-16**
22	IID+IIC vs ND	1	**2.1E-12**	1	1	**4.82E-74**	1	1	1	1	**1.66E-27**
23	IID+IIC vs LES	1	**0.0015**	1	1	**2.72E-34**	1	1	1	1	**1.62E-14**
24	IID+IIC vs DSIFT	1	0.27815	0.87827	1	**3.35E-91**	1	1	1	1	**1.43E-22**
25	IID+IIC vs IID+LAP	1	**1E-14**	**0.03207**	0.102185	**5.11E-77**	1	1	1	1	**9.34E-26**
26	IID+IIC vs IID+IHS	1	**1.5E-12**	**0.00025**	1	**1.5E-104**	1	1	1	1	**1.02E-35**
27	IID+IHS vs LAP	1	1	0.34819	1	**1.96E-08**	1	1	1	1	0.86365
28	IID+IHS vs DWT	1	1	**0.01209**	1	**9.26E-17**	1	1	1	1	0.143812
29	IID+IHS vs CVT	0.876168782	1	0.20541	1	**8.3E-27**	1	1	1	1	**0.002551**
30	IID+IHS vs COT	**3.61207E-11**	0.84806	**5.4E-08**	1	**2.83E-08**	1	1	1	1	1
31	IID+IHS vs NSCT	**1.46902E-10**	**3.6E-11**	**5.5E-08**	**3.41E-06**	**8.86E-11**	1	**0.001239**	1	1	0.898212
32	IID+IHS vs ST	**0.025516064**	1	1	1	**2.53E-06**	1	1	1	1	1
33	IID+IHS vs SVT	1	1	1	1	1	1	1	1	1	1
34	IID+IHS vs GFF	1	1	1	1	**8.67E-37**	1	1	1	1	**5.31E-07**
35	IID+IHS vs ND	1	1	0.18753	1	**1.86E-10**	1	1	1	1	1
36	IID+IHS vs LES	1	**0.0318**	0.98412	1	**5.43E-45**	1	1	1	1	**3.11E-08**
37	IID+IHS vs DSIFT	1	**8.3E-05**	1	1	0.116824	1	1	1	1	0.009156
38	IID+IHS vs IID+PCA	1	1	1	1	**1.41E-08**	1	1	1	1	0.289271
39	IID+IHS vs IID+IIC	1	**1.5E-12**	**0.00025**	1	**1.5E-104**	1	1	1	1	**1.02E-35**

performance differences. Given a set of 14 methods, the first step in statistical analysis is to use non-parametric Friedman test for ranking the performance of the methods presented in Table 4. At the bottom of each column in the table, the statistic for the Friedman test and its corresponding *p*-value is reported. In Table 4, it can be easily observed that

TABLE 6. Performance comparison with the post Bonferroni-Dunn test (statistical significance). The symbol "1", "0", or "−1" means that the proposed method is statistically (with 95% confidence) better, indistinguishable, or worse than the corresponding method.

Method	Metrics	LAP	DWT	CVT	COT	NSCT	ST	SVT	GFF	ND	LES	DSIFT	IID+IIC	IID+IHS
IID+PCA	SSIM	0	0	0	1	1	0	0	0	0	0	0	0	0
	IWSSIM	0	0	0	0	1	0	0	0	1	1	0	1	0
	MI	0	0	0	1	1	0	0	0	0	0	0	1	0
	GSM	0	0	0	0	1	0	0	0	0	0	0	0	0
	VSNR	0	0	-1	0	0	0	-1	-1	0	-1	0	-1	1
													IID+PCA	IID+IHS
IID+IIC	SSIM	0	0	0	1	1	0	0	0	0	0	0	0	0
	IWSSIM	-1	-1	-1	-1	0	-1	-1	-1	-1	-1	0	-1	-1
	MI	0	0	0	0	0	0	-1	0	0	0	0	-1	-1
	GSM	0	0	0	0	1	0	0	0	0	0	0	0	0
	VSNR	1	1	1	1	1	1	1	1	1	1	1	1	1
													IID+PCA	IID+IIC
IID+IHS	SSIM	0	0	0	1	1	1	0	0	0	0	0	0	0
	IWSSIM	0	0	0	0	1	0	0	0	0	1	1	0	1
	MI	0	1	0	1	1	0	0	0	0	0	0	0	1
	GSM	0	0	0	0	1	0	0	0	0	0	0	0	0
	VSNR	-1	-1	-1	-1	-1	-1	0	-1	-1	-1	0	-1	-1
													IID+IIC	IID+IHS
IID+PCA	IWSSIM	0	0	0	0	1	0	0	0	0	0	0	0	0
	VSNR	0	0	0	0	0	0	1	0	0	-1	0	-1	0
													IID+PCA	IID+IHS
IID+IIC	IWSSIM	0	0	0	0	0	0	0	0	0	0	0	0	0
	VSNR	1	1	1	1	1	1	1	1	1	1	1	1	1
													IID+PCA	IID+IIC
IIID+IHS	IWSSIM	0	0	0	0	1	0	0	0	0	0	0	0	0
	VSNR	0	0	-1	0	0	0	0	-1	0	-1	-1	0	-1

the proposed methods: IID+PCA, IID+IIC, and IID+IHS are able to obtain the highest rank (better rank is highlighted in boldface). As for the disease database, the proposed IID+PCA method performs better than the proposed IID+IHS and IID+IIC methods. On the other side, the proposed IID+IHS method is better than the proposed IID+PCA and IID+IIC methods for the robustness database.

The second step is to use the post hoc Bonferroni-Dunn test for detecting the cases in which the best performing method exhibited a significant performance difference from the others. The result of the post hoc Bonferroni-Dunn tests for the Friedman are presented in Tables 5-6. Statistically significant are marked in boldface. As the adjusted p-values in Table 5(the value $p < 0.05$ is highlighted in boldface) suggest, the post hoc Bonferroni-Dunn's procedure rejects hypotheses 31 for five objective metrics. Comparing the adjusted p-values in columns 7 and 12 (*VSNR* metric), the post hoc analysis rejects most of the hypotheses (3, 7, 8, 10, 12-32, and 34-39) on disease database, and (7, 10, 12-26, 29, 34, 36, and 39) on robustness database. Furthermore, for the significance differences, we list the detailed information in Table 6, where the symbol "1", "0", or "−1" denotes that the proposed method is statistically (with 95% confidence) better, indistinguishable, or worse that the corresponding method, respectively. As shown in Table 6, the proposed IID+IIC method in terms of the *VSNR* metric significantly outperforms all other methods on the two databases: disease and robustness. As for the disease database, it is found that

the proposed IID+IHS method in terms of the *MI* metric performs better than DWT, COT, NSCT, and IID+IIC methods. And the proposed IID+PCA method performs better than NSCT, ND, LES, and IID+IIC for the metric *IWSSIM*. However, IID+IIC method performs very worse for the metric *IWSSIM* for the two databases.

V. CONCLUSIONS

This paper primarily aims at showing that IID, which models the function of human vision, works well for medical image decomposition. We have presented three fusion methods based on IID models: Algorithm 1 and Algorithm 2. The proposed image decomposition schemes can make full use of the mechanism of visual cortex model to extract the illumination image and reflectance image from the input source MRI image and to extract color constancy to separate the PET input image into normal image and lesion image. Compared with other widely used MRI-PET medical image fusion methods, experiments carried on real medical imaging data show the outstanding performance of the proposed methods including IID+PCA, IID+IIC and IID+IHS, compared to the other state-of-the-arts fusion methods that consume more computation resource. Additionally, among the proposed three methods in this paper, IID+PCA method achieves the best performance by introducing enhanced structural information while less color distortion in the final fused image and by the well balance between the performance (Tables 2, 4-6) and computation complexity (Table 3), as well.

Although the proposed methods have shown good performance, there is a lot of future work to be continued. (1) PCA, IIC, and IHS are selected as the fusion rules for combing the IID decomposed images. However, there exist strong dependencies between IID coefficients of the intra-scale and inter-scale. In the future, we will design an adaptive fusion rule to make full use of the dependencies of the IID coefficients [56]. (2) The objective image fusion quality metrics can only measure the fused images from a limited perspective. For example, IID+IIC method performs best in terms of *VSNR* metric on the two databases: disease and robustness while the result images in figures could not preserve the salient information from the input images. In the future, we will use deep neural networks to design the metrics for evaluating functional information in the result fused images [57], [58].

REFERENCES

[1] H.-P. Schlemmer *et al.*, "Simultaneous MR/PET imaging of the human brain: Feasibility study," *Radiology*, vol. 248, no. 3, pp. 1028–1035, Sep. 2008.

[2] M. S. Judenhofer, "PET/MR images acquired with a compact MR-compatible PET detector in a 7-T magnet," *Radiology*, vol. 244, no. 3, pp. 807–814, Sep. 2007.

[3] M. Hofmann *et al.*, "MRI-based attenuation correction for PET/MRI: A novel approach combining pattern recognition and atlas registration," *J. Nucl. Med.*, vol. 49, no. 11, pp. 1875–1883, Nov. 2016.

[4] A. P. James and B. V. Dasarathy, "Medical image fusion: A survey of the state of the art," *Inf. Fusion*, vol. 19, pp. 4–19, Sep. 2014.

[5] R. Shen, I. Cheng, and A. Basu, "Cross-scale coefficient selection for volumetric medical image fusion," *IEEE Trans. Biomed. Eng.*, vol. 60, no. 4, pp. 1069–1079, Apr. 2013.

[6] V. S. Petrovic and C. S. Xydeas, "Gradient-based multiresolution image fusion," *IEEE Trans. Image Process.*, vol. 13, no. 2, pp. 228–237, Feb. 2004.

[7] V. D. Calhoun and T. Adalî, "Feature-based fusion of medical imaging data," *IEEE Trans. Inf. Technol. Biomed.*, vol. 13, no. 5, pp. 711–720, Sep. 2009.

[8] X. Kang, S. Li, L. Fang, and J. A. Benediktsson, "Intrinsic image decomposition for feature extraction of hyperspectral images," *IEEE Trans. Geosci. Remote Sens.*, vol. 53, no. 4, pp. 2241–2253, Apr. 2015.

[9] R. Vijayarajan and S. Muttan, "Iterative block level principal component averaging medical image fusion," *Optik*, vol. 125, no. 17, pp. 4751–4757, Sep. 2014.

[10] J. Umer and R. M. Muhammand, "MRI and PET image fusion using fuzzy logic and image local features," *Sci. World J.*, vol. 2014, Jan. 2014, Art. no.708075.

[11] Y. Liu, S. Liu, and Z. Wang, "Multi-focus image fusion with dense SIFT," *Inf. Fusion*, vol. 23, pp. 139–155, May 2015.

[12] T. Te-Ming, S. Shun-Chi, S. Hsuen-Chyun, and S. H. Ping, "A new look at IHS-like image fusion methods," *Inf. Fusion*, vol. 2, no. 3, pp. 177–186, Sep. 2001.

[13] J. Burt and E. Adelson, "The Laplacian pyramid as a compact image code," *IEEE Trans. Commun.*, vol. 31, no. 4, pp. 532–540, Apr. 1983.

[14] S. Zheng, W. Z. Shi, J. Liu, G. X. Zhu, and J. W. Tian, "Multisource image fusion method using support value transform," *IEEE Trans. Image Process.*, vol. 16, no. 7, pp. 1831–1839, Jul. 2007.

[15] H. Zhao, Z. Shang, Y. Y. Tang, and B. Fang, "Multi-focus image fusion based on the neighbor distance," *Pattern Recognit.*, vol. 46, pp. 1002–1011, Mar. 2013.

[16] G. Pajares and J. M. de la Cruz, "A wavelet-based image fusion tutorial," *Pattern Recognit.*, vol. 37, no. 9, pp. 1855–1872, 2004.

[17] R. Singh and A. Khare, "Fusion of multimodal medical images using daubechies complex wavelet transform—A multiresolution approach," *Inf. Fusion*, vol. 19, pp. 49–60, Sep. 2014.

[18] E. Candès, L. Demanet, D. Donoho, and X. Ying, "Fast discrete curvelet transforms," *Multiscale Model. Simul.*, vol. 5, no. 3, pp. 861–899, Sep. 2006.

[19] L. Yang, B. L. Guo, and W. Ni, "Multimodality medical image fusion based on multiscale geometric analysis of contourlet transform," *Neurocomputing*, vol. 72, nos. 1–3, pp. 203–211, 2008.

[20] R. Srivastava and A. Khare, "Multifocus noisy image fusion using contourlet transform," *Imag. Sci. J.*, vol. 63, no. 7, pp. 408–422, Jul. 2015.

[21] X.-B. Qu, J.-W. Yan, H.-Z. Xiao, and Z.-Q. Zhu, "Image fusion algorithm based on spatial frequency-motivated pulse coupled neural networks in nonsubsampled contourlet transform domain," *Acta Autom. Sin.*, vol. 34, no. 12, pp. 1508–1514, 2008.

[22] G. Easley, D. Labate, and W.-Q. Lim, "Sparse directional image representations using the discrete shearlet transform," *Appl. Comput. Harmon. Anal.*, vol. 25, no. 1, pp. 25–46, Jul. 2008.

[23] Q.-G. Miao, C. Shi, P.-F. Xu, M. Yang, and Y. B. Shi, "A novel algorithm of image fusion using shearlets," *Opt. Commun.*, vol. 284, no. 6, pp. 1540–1547, Mar. 2011.

[24] L. Wang, B. Li, and L.-F. Tian, "Multi-modal medical image fusion using the inter-scale and intra-scale dependencies between image shift-invariant shearlet coefficients," *Inf. Fusion*, vol. 19, no. 9, pp. 20–28, 2014.

[25] L. Wang, B. Li, and L. F. Tian, "EGGDD: An explicit dependency model for multi-modal medical image fusion in shift-invariant shearlet transform domain," *Inf. Fusion*, vol. 19, pp. 29–37, Sep. 2013.

[26] S. Li, X. Kang, and J. Hu, "Image fusion with guided filtering," *IEEE Trans. Image Process.*, vol. 22, no. 7, pp. 2864–2875, Jul. 2013.

[27] K. He, J. Sun, and X. Tang, "Guided image filtering," *IEEE Trans. Pattern Anal. Mach. Intell.*, vol. 35, no. 6, pp. 1397–1409, Jun. 2013.

[28] K. Subr, C. Soler, and F. Durand, "Edge-preserving multiscale image decomposition based on local extrema," *ACM Trans. Graph.*, vol. 28, no. 5, p. 147, Dec. 2009.

[29] Z. Xu, "Medical image fusion using multi-level local extrema," *Inf. Fusion*, vol. 19, no. 11, pp. 38–48, 2013.

[30] S. Daneshvar and H. Ghassemian, "MRI and PET image fusion by combining IHS and retina-inspired models," *Inf. Fusion*, vol. 11, no. 2, pp. 114–123, 2010.

[31] Z. Xiaoli, L. Xiongfei, F. Yuncong, Z. Haoyu, and L. Zhaojun, "Image fusion with internal generative mechanism," *Expert Syst. Appl.*, vol. 42, no. 5, pp. 2382–2391, Apr. 2015.

[32] F. Kou, Z. Wei, W. Chen, X. Wu, C. Wen, and Z. Li, "Intelligent detail enhancement for exposure fusion," *IEEE Trans. Multimedia*, vol. 20, no. 2, pp. 484–495, Feb. 2018.

[33] W. Zhao, H. Lu, and D. Wang, "Multisensor image fusion and enhancement in spectral total variation domain," *IEEE Trans. Multimedia*, vol. 20, no. 4, pp. 866–879, Apr. 2018.

[34] J. H. Jang, Y. Bae, and J. B. Ra, "Contrast-enhanced fusion of multisensor images using subband-decomposed multiscale retinex," *IEEE Trans. Image Process.*, vol. 21, no. 8, pp. 3479–3490, Aug. 2012.

[35] Z. U. Rahman, D. J. Jobson, and G. A. Woodell, "Multisensor fusion and enhancement using the Retinex image enhancement algorithm," *Proc. SPIE*, vol. 4736, Jul. 2012, Art. no. 477590.

[36] L. Shen, C. Yeo, and B.-S. Hua, "Intrinsic image decomposition using a sparse representation of reflectance," *IEEE Trans. Pattern Anal. Mach. Intell.*, vol. 35, no. 12, pp. 2904–2915, Dec. 2013.

[37] C. O. Ancuti and C. Ancuti, "Single image dehazing by multi-scale fusion," *IEEE Trans. Image Process.*, vol. 22, no. 8, pp. 3271–3282, Aug. 2013.

[38] J. Shen, X. Yang, X. Li, and Y. Jia, "Intrinsic image decomposition using optimization and user scribbles," *IEEE Trans. Cybern.*, vol. 43, no. 2, pp. 425–436, Apr. 2013.

[39] H. R. V. Joze and M. S. Drew, "Exemplar-based color constancy and multiple illumination," *IEEE Trans. Pattern Anal. Mach. Intell.*, vol. 36, no. 5, pp. 860–873, May 2013.

[40] P. V. Gehler, C. Rother, and A. Blake, "Bayesian color constancy revisited," in *Proc. IEEE Conf. Vis. Pattern Recognit.*, Jun. 2008, pp. 1–8.

[41] W. Ma, J. M. Morel, S. Osher, and A. Chien, "An L₁-based variational model for Retinex algorithm and its application to medical images," *IEEE Comput. Vis. Pattern Recognit.*, Jun. 2011, pp. 153–160.

[42] A. Buades, T. M. Le, J. M. Morel, and L. A. Vese, "Fast cartoon + texture image filters," *IEEE Trans. Image Process.*, vol. 19, no. 8, pp. 1978–1986, Aug. 2010.

[43] J. V. D. Weijer, C. Schmid, and J. Verbeek, "Using high-level visual information for color constancy," in *Proc. IEEE Int. Conf. Comput. Vis.*, Oct. 2007, pp. 1–8.

[44] K. A. Johnson and J. A. Becker. (2011). *The Whole Brain Altas*. [Online]. Available: http://www.med.harvard.edu/aanlib/

[45] C. Ciprian, D. Alexander, H. Wolf-Dieter, and R. R. Bruce, "PET/MRI for neurologic applications," *J. Nucl. Med.*, vol. 53, no. 12, pp. 1916–1925, 2016.

[46] Z. Wang, A. C. Bovik, H. R. Sheikh, and E. P. Simoncelli, "Image quality assessment: From error visibility to structural similarity," *IEEE Trans. Image Process.*, vol. 13, no. 4, p. 612, Apr. 2004.

[47] Z. Wang and Q. Li, "Information content weighting for perceptual image quality assessment," *IEEE Trans. Image Process.*, vol. 20, no. 5, pp. 1185–1198, May 2011.

[48] M. Hossny, S. Nahavandi, and D. Creighton, "Comments on 'Information measure for performance of image fusion, *Electron. Lett.*, vol. 44, no. 18, pp. 1066–1067, Aug. 2008.

[49] A. Liu, W. Lin, and M. Narwaria, "Image quality assessment based on gradient similarity," *IEEE Trans. Image Process.*, vol. 21, no. 4, pp. 1500–1512, Apr. 2012.

[50] D. M. Chandler and S. S. Hemami, "VSNR: A wavelet-based visual signal-to-noise ratio for natural images," *IEEE Trans. Image Process.*, vol. 16, no. 9, pp. 2284–2298, Sep. 2007.

[51] J. Farrell, M. Parmar, and B. Wandell, "Using visible SNR (vSNR) to compare the image quality of pixel binning and digital resizing," in *Proc. Conf. Paper*, Jan. 2010, pp. 217–222.

[52] O. Dietrich, S. Heiland, T. Benner, and K. Sartor, "Reducing motion artefacts in diffusion-weighted MRI of the brain: Efficacy of navigator echo correction and pulse triggering," *Diagnostic Neuroradiol.*, vol. 42, no. 2, pp. 85–91, Feb. 2000.

[53] P. T. Yap and P. Raveendran, "Image focus measure based on Chebyshev moments," *IEE Proc. Vis., Image Signal Process.*, vol. 151, no. 2, pp. 128–136, Apr. 2004.

[54] M. Z. Ali, N. H. Awad, and P. N. Suganthan, "A novel hybrid Cultural Algorithms framework with trajectory-based search for global numerical optimization," *Inf. Sci.*, vols. 334–335, pp. 219–249, Mar. 2015.

[55] A. Rusiecki, "Robust learning algorithm based on LTA estimator," *Neurocomputing*, vol. 120, pp. 624–632, Nov. 2013.

[56] H. M. Hu, J. Wu, and B. Li, "An adaptive fusion algorithm for visible and infrared videos based on entropy and the cumulative distribution of gray levels," *IEEE Trans. Multimedia*, vol. 19, no. 12, pp. 2706–2719, Dec. 2017.

[57] W. P. Segars, B. M. W. Tsui, C. Jing, F. F. Yin, G. S. K. Fumg, and E. Samei, "Application of the 4-D XCAT phantoms in biomedical imaging and beyond," *IEEE Trans. Med. Imag.*, vol. 37, no. 3, pp. 680–692, Mar. 2018.

[58] S. Bosse, D. Maniry, K. R. Müller, T. Wiegand, and W. Samek, "Deep neural networks for no-reference and full-reference image quality assessment," *IEEE Trans. Image Process.*, vol. 27, no. 1, pp. 206–219, Jan. 2018.

● ● ●